ORIGINAL ARTICLE

lajss.org© Latin American Journal of Solids and Structures

www.lajss.org

Equivalent Thickness Conversion and Perforation Morphology of Typical Metallic Target Plates under Fragment Impact

Chuanyun Tao[a], Wenbin Li[a]*, Yu Zheng[a], Ning Jiang[b], Peng Chen[c], Weihang Li[b]

[a] School of Mechanical Engineering, Nanjing University of Science and Technology, Nanjing 210094, Jiangsu, China. Email: tcy@njust.edu.cn, lwb2000cn@njust.edu.cn, zhengyu@njust.edu.cn
[b] Ningbo Branch, China Academy of Ordnance Science, Ningbo 315000, Zhejiang, China. Email: njustjn@163.com, lwh992190035@163.com
[c] Northwest Industrial Group Co., Ltd., Xi'an 710043, Shaanxi, China. Email: cp19981212@163.com

* Corresponding author

https://doi.org/10.1590/1679-7825/e9170

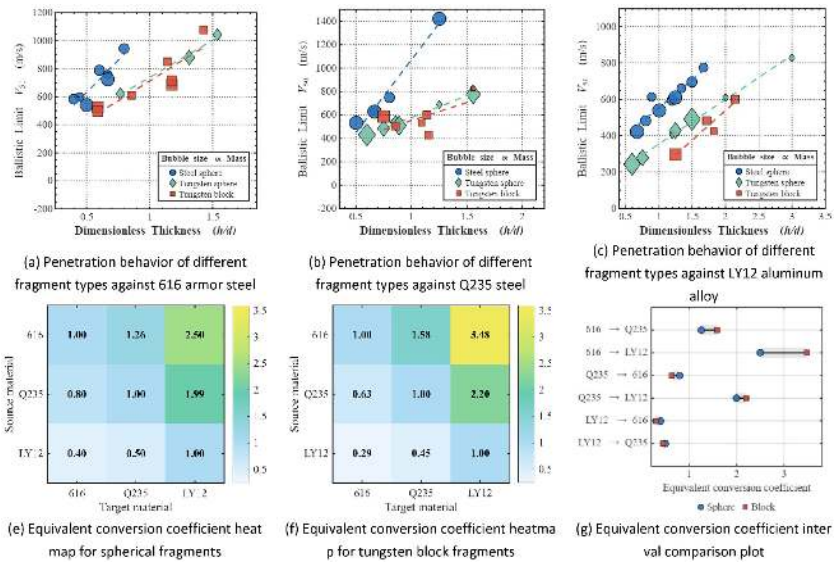
Abstract

Equivalent-thickness conversion among metallic targets is important for vulnerability assessment and protection modelling, but conventional coefficients are often treated as material constants and seldom include fragment morphology. Penetration tests were conducted on 616 armor steel, Q235 steel, and LY12 aluminum alloy using steel spheres, tungsten spheres, and tungsten block fragments. A V50-based database was established, and failure mechanisms were examined from perforation morphology, exit-side SEM, and metallography. A semi-empirical ballistic-limit model was developed from key variables, with a residual correction term to describe the coupled deviation between fragment geometry and target response. The corrected model achieved a mean absolute percentage error of 7.91% and a coefficient of determination of 0.852. The conversion matrices show strong dependence on fragment type. For 616 steel converted to LY12 aluminum alloy, the coefficient increases from 2.50 for spherical fragments to 3.48 for tungsten blocks, giving a morphology-induced deviation of 39.03%. Thus, conversion should be defined by fragment type and target material rather than by a single material constant.

Keywords

equivalent conversion coefficient; *V50* ballistic limit; fragment shape effect; target material; dimensional analysis; perforation mechanism

Graphical Abstract



(a) Penetration behavior of different fragment types against 616 armor steel

(b) Penetration behavior of different fragment types against Q235 steel

(c) Penetration behavior of different fragment types against LY12 aluminum alloy

(e) Equivalent conversion coefficient heat map for spherical fragments

(f) Equivalent conversion coefficient heatmap for tungsten block fragments

(g) Equivalent conversion coefficient interval comparison plot

Received June 17, 2026. In revised form July 03, 2026. Accepted July 05, 2026. Available online July 07, 2026
https://doi.org/10.1590/1679-7825/e9170

Latin American Journal of Solids and Structures. ISSN 1679-7825. Copyright © 2026. This is an Open Access article distributed under the terms of the Creative Commons Attribution license, which permits unrestricted use, distribution, and reproduction in any medium, provided the original work is properly cited.

1 INTRODUCTION

In target vulnerability analysis and damage assessment, typical homogeneous metallic plates are often used as equivalent substitutes for real target structures, since this reduces the complexity of numerical modeling and physical testing (Lomazzi et al., 2022; Li et al., 2020; Zhang and Li, 2022; Li et al., 2024; Li and Zhang, 2024). Among the reference materials most frequently used in this context, 616 high-hardness armor steel, Q235 low-carbon steel, and LY12 aluminum alloy are representative of armor protection structures, conventional ship structures/conventional hull structures and lightweight aerospace structures, respectively (Xiao et al., 2024; Du et al., 2025; Yu et al., 2025; Zhang et al., 2024). Even so, the ballistic-performance conversion scale among these three target materials remains unclear. In current cross-material equivalence calculations, engineering practice still relies largely on empirical estimates or conversions with limited theoretical support, which inevitably weakens confidence in vulnerability predictions. To reduce the dimensionality of cross-material calculations, dynamic ballistic equivalence has gradually replaced static conversion as a more relevant research focus. Xiao et al. (2024) derived an equivalent perforation prediction model for thin flat plates from dimensional analysis under the principle of equal ballistic limit velocity. Zhang et al. (2024) proposed a modified compensation-model method for similarity and equivalent design among dissimilar steel targets, improving conversion accuracy across material systems. Du et al. (2025) developed a rapid equivalence strategy for composite and metallic protection systems. Yu et al. (2025) further showed the nonlinear attenuation of typical steel-fragment velocity in snow, indicating that a robust cross-material conversion framework must account for dynamic coupling between the penetration load and boundary conditions. For inverse impact-parameter estimation and analytical modeling, Jordan and Naito (2010) proposed an empirical method for deriving impact velocity from penetration depth, while Wu et al. (2025) developed an analytical model for spherical-nosed projectiles perforating finite-thickness metallic plates. A series of analytical formulations by Masri, Schonberg and other authors addressed ductile hole growth, fragment-simulating projectile impact, adiabatic shear plugging, rigid-projectile perforation of thin plates and non-identical layered targets, thereby providing useful forms for engineering conversion (Masri, 2022; Schonberg and Ryan, 2022; Sen et al., 2022; Han et al., 2022; Yankelevsky et al., 2023; Masri and Ryan, 2023; Masri and Ryan, 2024).

From the perspective of damage assessment and vulnerability modeling, recent studies have moved beyond the ballistic resistance of a single plate toward modeling frameworks that better represent battlefield conditions, including fragment dispersion, fragment-target intersection, equivalent target plates and spatio-temporal sequences of multilayer fragments. Lomazzi et al. (2022) defined a vulnerability assessment procedure for aircraft platforms. Li et al. and Zhang and Li developed target-damage efficiency methods from the viewpoints of fragment dispersion, intersection mechanisms and equivalent-target-plate damage probability (Li et al., 2020; Zhang and Li, 2022; Li et al., 2024a; Li and Zhang, 2024). Zhu et al. (2019) reported the axial distribution of fragments from dynamically exploding metal shells, providing boundary inputs for subsequent fragment-threat parameterization and equivalence conversion.

The morphology of damaging fragments in real battlefield environments is complex and diverse, and fragment configuration strongly affects both target energy absorption and perforation failure. Ballistic experiments by Zhang et al. (2023) showed that, under the same initial kinetic energy, cubic fragments produced greater penetration depth and larger perforation area than spherical fragments, together with a lower ballistic limit velocity. Kpenyigba et al. (2013) likewise confirmed the decisive influence of projectile shape on the dynamic response and micro-failure evolution of metallic plates. Such morphology-induced load localization causes fragments with the same mass but different shapes to produce different damage efficiencies. In addition, target perforation resistance is inherently governed by dynamic constitutive behavior at very high strain rates. Børvik et al. (2009) systematically evaluated the ballistic limits of several high-strength steels under small-arms impact and clarified the dominant role of dynamic yield stress and strain hardening in penetration resistance. For lightweight aerospace alloys, Owolabi et al. (2007) analyzed adiabatic shear-band evolution in aluminum alloys under dynamic shear loading, providing a materials basis for understanding local thermal softening and brittle collapse in aluminum targets at high strain rates. Shin et al. (2018) and Mykhailovskyi et al. (2024) extended the discussion to larger structures by establishing ballistic test methods for modern naval structural materials and fragment-damage assessment methods for protective constructions. James (2020) further developed a model for assessing penetrating injuries from ballistic projectiles, broadening the engineering use of target-material effects.

Traditional semi-empirical or analytical models remain limited when they are used to handle the high-dimensional nonlinear interaction between morphology and material. Data-driven and surrogate models have recently shown clear advantages. Ryan et al. (2024) applied machine learning to the global prediction of terminal ballistics outcomes. To address the black-box nature of machine-learning models, Ekanayake et al. (2022) introduced the game-theoretic SHAP approach to quantify marginal feature contributions in engineering-material property prediction. At the same time, high-dimensional optimization strategies that combine design of experiments and response surface methodology have been successfully applied to high-hardness perforated armor-plate optimization and trajectory-correction projectile design (Kılıç et al., 2017; Xing et al., 2022; Thompson et al., 2022a; Thompson et al., 2022b), offering useful white-box fitting tools for complex penetration datasets. Dey et al. (2004), Rodríguez-Millán et al. (2018), Senthil et al. (2018) and Cheng et al. (2021, 2022) revealed strong coupling among projectile or fragment nose shape, target strength, impact velocity range and local damage evolution.

Their results indicate that fragments with different morphologies may trigger markedly different perforation mechanisms and ballistic limits even when mass or scale is similar. With the development of data-driven approaches, Ryan et al. (2016), Lei et al. (2021), Noh et al. (2025), Du et al. (2025) and Zhu et al. (2025) have used machine learning, physics-informed constraints and equivalence methods for ballistic-limit prediction, fragment-velocity distribution prediction and cross-material structural conversion, showing the advantage of coupling physical priors with data models in high-dimensional nonlinear problems.

In summary, existing studies have provided an important basis for ballistic limit research, fragment morphology effects, and equivalent modeling. However, thickness equivalence for target vulnerability assessment remains insufficiently addressed. Equivalent coefficients are usually determined according to material strength, density, or empirical formulas, implicitly assuming that variations in fragment morphology do not alter the material conversion relationship. This assumption makes it difficult to explain the differences in failure modes induced by spherical and block-shaped fragments in different target materials. Based on this consideration, steel spheres, tungsten spheres, and tungsten block fragments were selected as typical damage elements in this study, and penetration experiments were conducted on three metallic target materials. In actual explosive fragment fields, block-shaped fragments usually impact targets with uncertain attitudes. Therefore, this study does not further distinguish their specific face-, edge-, or corner-impact states, but treats them as typical non-spherical fragments for engineering statistical analysis. The main objective is to investigate how the thicknesses of different metallic target plates can be equivalently converted under the impact of different typical fragments, and to what extent fragment morphology differences modify the material equivalence relationship.

2 EXPERIMENTAL PROGRAM AND METHODS

2.1 Target-material characterization

Three typical target materials were used: 616 high-hardness armor steel, Q235 low-carbon structural steel and LY12 aluminum alloy. All plates had an in-plane size of 500 mm × 500 mm. Plate thicknesses of 4, 6, 8, 10, 12 and 15 mm were selected to cover the typical range from thin to medium-thickness plates for equivalent conversion. The density, yield strength, ultimate tensile strength, elongation and hardness of the three materials are listed in Table 1.

Table 1 Quasi-static mechanical properties of target materials.

Material	Density (g/cm³)	Yield strength (MPa)	Ultimate tensile strength (MPa)	Elongation (%)	Hardness (HB)
616	7.85	1250	1650	10	450
Q235	7.85	235	410	26	120
LY12	2.78	325	460	17	120

2.2 Fragment parameters

The fragments used in the tests included steel spheres made of 45 steel, tungsten spheres made of 93W alloy, and tungsten block fragments. Their parameters are summarized in Table 2.

Table 2 Summary of fragment parameters.

Type	Material	Density (g/cm³)	Dimensions (mm)	Mass (g)
Steel sphere	45 Steel	7.85	Φ9, Φ10, Φ12	2.93, 4.09, 6.99
Tungsten sphere	93W	17.60	Φ4.8, Φ5, Φ6.5, Φ7, Φ7.6, Φ8, Φ10	1.03, 1.15, 2.60, 3.17, 4.00, 4.72, 9.22
Tungsten block fragment	93W	17.60	3.85×3.85×3.85, 5.5×5.5×5.5, 5.2×5.2×8, 7×7×4.7, 8×8×8, 8.5×8.5×6.5, 8.5×7.5×6	0.98, 2.86, 3.75, 4.00, 6.80, 8.20, 8.80

2.3 Penetration test setup, method, and data processing

Fragments were launched using a 14.5 mm ballistic gun, and the initial fragment velocity was controlled by adjusting the propellant charge. A high-speed photographic velocity-measurement system was used to measure the impact velocity and residual velocity of the fragments. The target plate was rigidly fixed on a support using a clamping fixture to ensure normal impact. A schematic diagram of the experimental setup is shown in Figure 1. As shown in Figure 3, the incident velocity refers to the velocity at the target surface. The high-speed photography measurement window was arranged in

the near-field region in front of the target. The incident velocity was obtained by extrapolating the displacement of the fragment in consecutive pre-target frames to the target-surface position. Therefore, the velocity attenuation caused by air resistance between the measurement point and the target surface was already considered during the determination of the target-surface velocity.

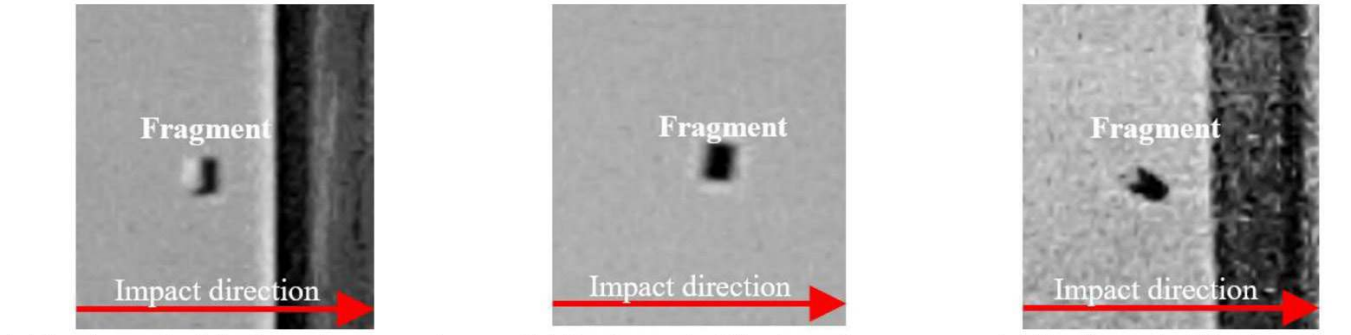
For tungsten block fragments, the impact attitude affects the local contact area, stress concentration state, and perforation response. The purpose of this study is not to establish separate penetration laws for tungsten block fragments under face-on, edge-on, or corner-on impact attitudes. Instead, the tungsten block is treated as a typical non-spherical fragment to analyze its influence on the equivalent-thickness conversion relationship among metallic target materials. Therefore, in the experimental data processing, the specific impact attitude of each tungsten block fragment was not classified, nor were the tungsten block fragments divided into fixed-attitude test conditions. During high-speed photographic velocity measurement, the primary requirement was to ensure that the fragment velocity direction was approximately consistent with the target normal, and the target-surface velocity was obtained by extrapolating the displacement from consecutive pre-target frames.

For tungsten block fragments, if the high-speed images showed obvious tumbling, sudden lateral attitude change, abnormal flight trajectory, or unstable velocity extrapolation, that shot was used only to observe the perforation phenomenon and was not included in the *V50* statistics. For valid tests without the above obvious abnormalities, the data were uniformly included in the *V50* fitting of tungsten block fragments. All cases shown in Figure 2 were included in the statistical test conditions. Therefore, the obtained *V50* of tungsten block fragments does not correspond to a deterministic ballistic limit under a specific fixed impact attitude, but represents the average response of valid samples without attitude classification in an engineering statistical sense.



(a) Schematic diagram of the experimental setup (b) Test-site layout

Figure 1. Experimental setup for normal penetration tests



(a) Pre-impact attitude under normal impact (b) Pre-impact attitude under approximately normal impact (c) Pre-impact attitude under oblique impact

Figure 2. High-speed images showing pre-impact attitudes of tungsten block fragments

The *V50* ballistic limit velocity was obtained using the staircase method. For each test condition, at least 10 valid impacts were recorded. An estimated initial velocity was first assigned; when complete perforation occurred, the subsequent velocity was reduced, and otherwise it was increased. The velocity increment was set to 5% of the estimated *V50*. During post-processing, a logistic regression model was used to fit the relation between perforation probability and impact velocity (Mauchant et al., 2011).

It is assumed that the perforation probability *P* follows: $p = 1/\left\{1+\exp\left[-(V_i-u)/\sigma\right]\right\}$, where μ denotes the ballistic limit velocity *V50*, at which the perforation probability is 0.5, and σ is the scale parameter. The parameters μ and σ were determined by maximum likelihood estimation.

Representative test processes are shown in Figure 3.

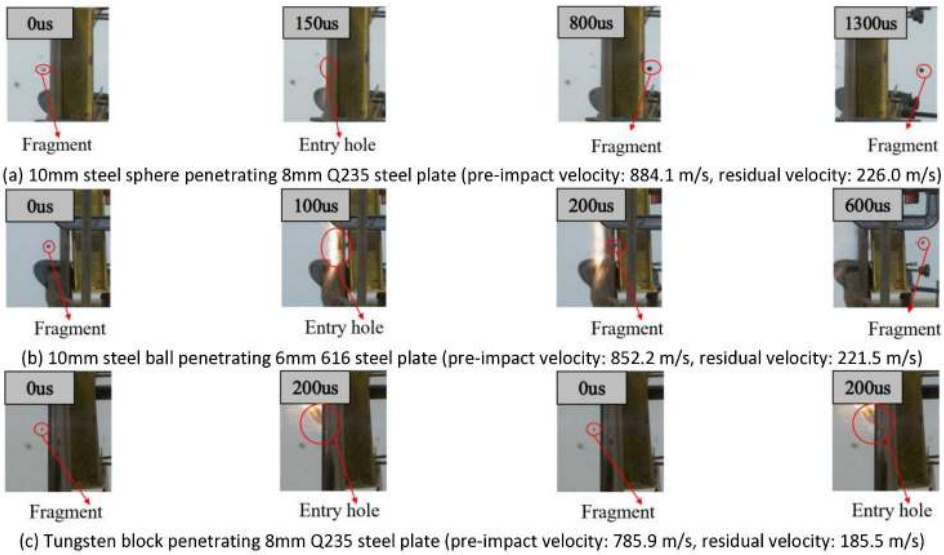


Figure 3. Representative normal-penetration tests of selected fragments against selected target materials

3 RESULTS

3.1 *V50* ballistic limit data

After data processing, the *V50* values for all test conditions were obtained and are listed in Tables 3-5.

Table 3 Experimental V50 results for steel spherical fragments.

Target	Thickness *h* (mm)	Diameter *d* (mm)	Mass *m* (g)	*V50* (m/s)
616 steel	4	9.0	2.93	600.3
616 steel	6	9.0	2.93	759.9
616 steel	4	10.0	4.09	585.4
616 steel	6	10.0	4.09	789.9
616 steel	8	10.0	4.09	942.9
616 steel	6	12.0	6.99	542.0
616 steel	8	12.0	6.99	724.9
LY12 aluminum alloy	8	9.0	2.93	612.5
LY12 aluminum alloy	12	9.0	2.93	661.1
LY12 aluminum alloy	15	9.0	2.93	775.0
LY12 aluminum alloy	8	10.0	4.09	481.5
LY12 aluminum alloy	12	10.0	4.09	596.1
LY12 aluminum alloy	15	10.0	4.09	695.4
LY12 aluminum alloy	8	12.0	6.99	422.5
LY12 aluminum alloy	12	12.0	6.99	539.5
LY12 aluminum alloy	15	12.0	6.99	609.8
Q235 steel	6	9.0	2.93	637.5
Q235 steel	8	10.0	4.09	745.8
Q235 steel	6	12.0	6.99	529.8
Q235 steel	8	12.0	6.99	629.2
Q235 steel	15	12.0	6.99	1420.1

Table 4 Experimental V50 results for tungsten spherical fragments.

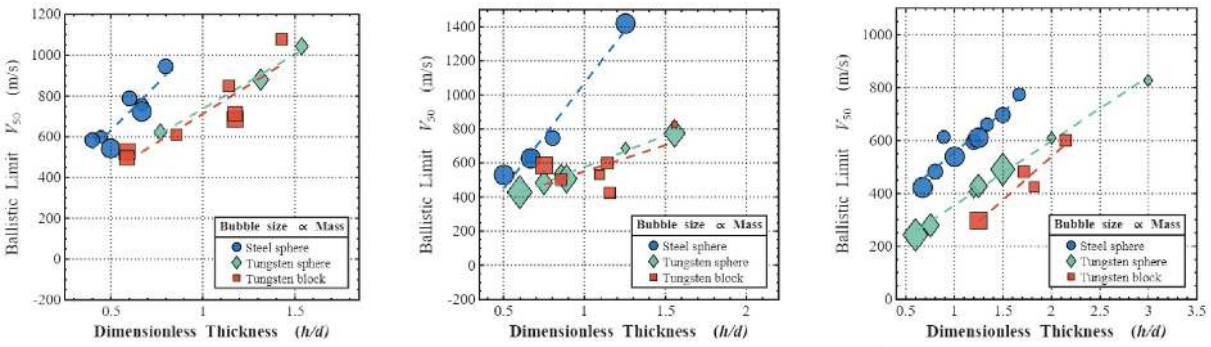
Target	Thickness *h* (mm)	Diameter *d* (mm)	Mass *m* (g)	*V50* (m/s)
616 steel	5	6.5	2.60	622.3
616 steel	10	6.5	2.60	1042.5
616 steel	10	7.6	4.00	878.2
LY12 aluminum alloy	6	5.0	1.15	407.0
LY12 aluminum alloy	6	8.0	4.72	280.0
LY12 aluminum alloy	6	10.0	9.22	244.0
LY12 aluminum alloy	10	5.0	1.15	610.0
LY12 aluminum alloy	10	8.0	4.72	428.0
LY12 aluminum alloy	15	5.0	1.15	827.0
LY12 aluminum alloy	15	10.0	9.22	490.0
Q235 steel	6	4.8	1.03	685.9
Q235 steel	6	7.0	3.17	533.3
Q235 steel	6	8.0	4.75	486.1
Q235 steel	6	10.0	9.31	428.8
Q235 steel	8	9.0	6.73	505.6
Q235 steel	14	9.0	6.73	776.4

Table 5 Experimental V50 results for tungsten block fragments.

Target	Thickness *h* (mm)	Characteristic size *d* (mm)	Mass *m* (g)	*V50 (m/s)*
616 steel	5	8.5	8.20	527.2
616 steel	10	8.5	8.20	685.5
616 steel	5	8.5	6.80	495.5
616 steel	10	8.5	6.80	711.9
616 steel	6	7.0	4.00	610.3
616 steel	8	7.0	4.00	851.4
616 steel	10	7.0	4.00	1079.1
LY12 aluminum alloy	10	5.5	2.87	424.0
LY12 aluminum alloy	10	8.0	8.82	296.5
LY12 aluminum alloy	12	7.0	4.00	481.5
LY12 aluminum alloy	15	7.0	4.00	601.5
Q235 steel	6	3.9	0.99	826.5
Q235 steel	6	5.5	2.86	532.0
Q235 steel	6	5.2	3.75	425.5
Q235 steel	6	8.0	8.82	585.6
Q235 steel	6	7.0	4.00	504.0
Q235 steel	8	7.0	4.00	597.9

Note: In Table 5, the characteristic dimension *d* of the tungsten block fragment refers to its side length. For non-cubic tungsten block fragments / non-equiaxed tungsten block fragments, *d* was taken as the contact side length, while the mass *m* was determined from direct measurements. Since the specific face-on, edge-on, or corner-on impact attitude of each tungsten block fragment was not classified in the experiments, the *V50* values listed in the table represent the engineering statistical ballistic limit velocities of tungsten block fragments samples without attitude classification, rather than deterministic *V50* values under a single fixed impact attitude.

Tables 3-5 show that, within comparable ranges of target material, thickness and fragment mass, the overall penetration capability follows the order tungsten block fragments > tungsten spheres > steel spheres. For example, for a 6 mm thick 616 armor-steel plate, a steel sphere with m = 4.09 g and d = 10 mm gives *V50* = 789.9 m/s, whereas a tungsten block fragment with a comparable mass scale with m = 4.00 g and d = 7 mm gives *V50* = 610.3 m/s. This indicates the stronger localized loading capability of high-density angular fragments. This ordering is affected jointly by fragment mass, characteristic size and contact attitude; therefore, it should not be extrapolated as an absolute rule for all size and velocity ranges. Under the same or similar threat conditions, the target perforation resistance generally follows the order 616 steel > Q235 steel > LY12 aluminum alloy. To clarify the nonlinear coupling between fragment geometry and target material, the dimensionless thickness *h/d* was introduced as a key geometric scale. A multidimensional scatter mapping of fragment mass, dimensionless thickness and *V50* was then used to analyze the penetration response of the three metallic target materials separately.



(a) Penetration behavior of different fragment types against 616 armor steel

(b) Penetration behavior of different fragment types against Q235 steel

(c) Penetration behavior of different fragment types against LY12 aluminum alloy

Figure 4. Penetration response characteristics of different fragments against different target plates

As shown in Figure 4, for fragments with different morphologies and materials normally impacting 616 armor steel, Q235 steel, and LY12 aluminum-alloy plates, the ballistic limit velocity V50 generally increases with increasing dimensionless thickness h/d. The bubble size in the figure represents the fragment mass and is used to help identify the influence of mass scale on local deviations.

Owing to its higher yield strength and hardness, 616 armor steel exhibits the highest overall ballistic limit, whereas LY12 aluminum alloy shows a relatively lower perforation threshold because of its lower density and strength. Compared with steel spheres, tungsten-alloy fragments have a higher density and a stronger capability for local momentum concentration. The physical role of the mass term is not identical for different target materials. For high-strength 616 steel, an increase in fragment mass is more likely to enhance localized shearing and plugging-type energy dissipation. For low-resistance LY12 aluminum alloy, however, the mass effect is more readily manifested as hole-edge expansion, material uplift, and enlargement of the ductile tearing region.

3.2 Failure morphology and mechanisms

Exit-side failure features of different fragment-target combinations were analyzed using macroscopic perforation morphology, SEM images of the exit-side hole edge, and metallographic comparison between the near-hole region a and the far-field base-material region b. The results are presented in Figures 5-7.

Figures 5-7 present the macroscopic perforation morphology, exit-hole-edge SEM images and near-hole/far-field metallographic features after tungsten block fragments, steel spheres and tungsten spheres penetrated Q235 steel, 616 armor steel and LY12 aluminum-alloy plates. The macroscopic and microscopic images are arranged according to target material and fragment type. In the metallographic images, region a denotes the near-hole region, while region b denotes the base material away from the perforation.

The macroscopic perforation morphology shows clear differences in exit-side response among the target materials. Under all three fragment types, Q235 steel forms a distinct plastic deformation zone around the hole edge; local petalling, tensile tearing and irregular hole enlargement are visible near the exit, indicating substantial plastic flow during perforation. In 616 armor steel, the exit hole is generally more compact, while edge curling and large-scale plastic bulging are strongly suppressed. This indicates that the high-strength target constrains circumferential plastic expansion more effectively and that exit-side failure becomes more localized. By contrast, LY12 aluminum alloy shows the most pronounced edge curling, material uplift and local tearing, suggesting that a low-resistance, high-ductility target more readily undergoes wide-range plastic hole enlargement under impact loading.

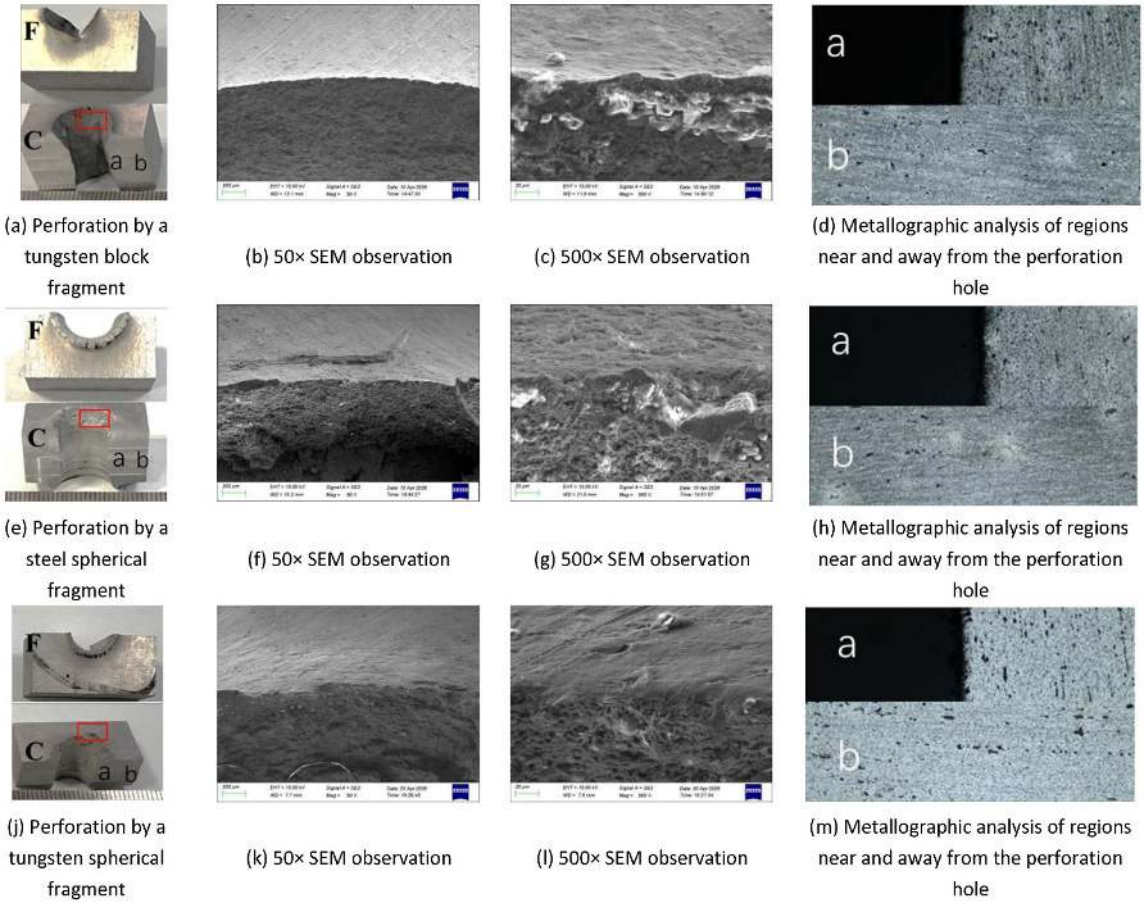


Figure 5. Perforation analysis of the three fragment types against the LY12 aluminum alloy plate

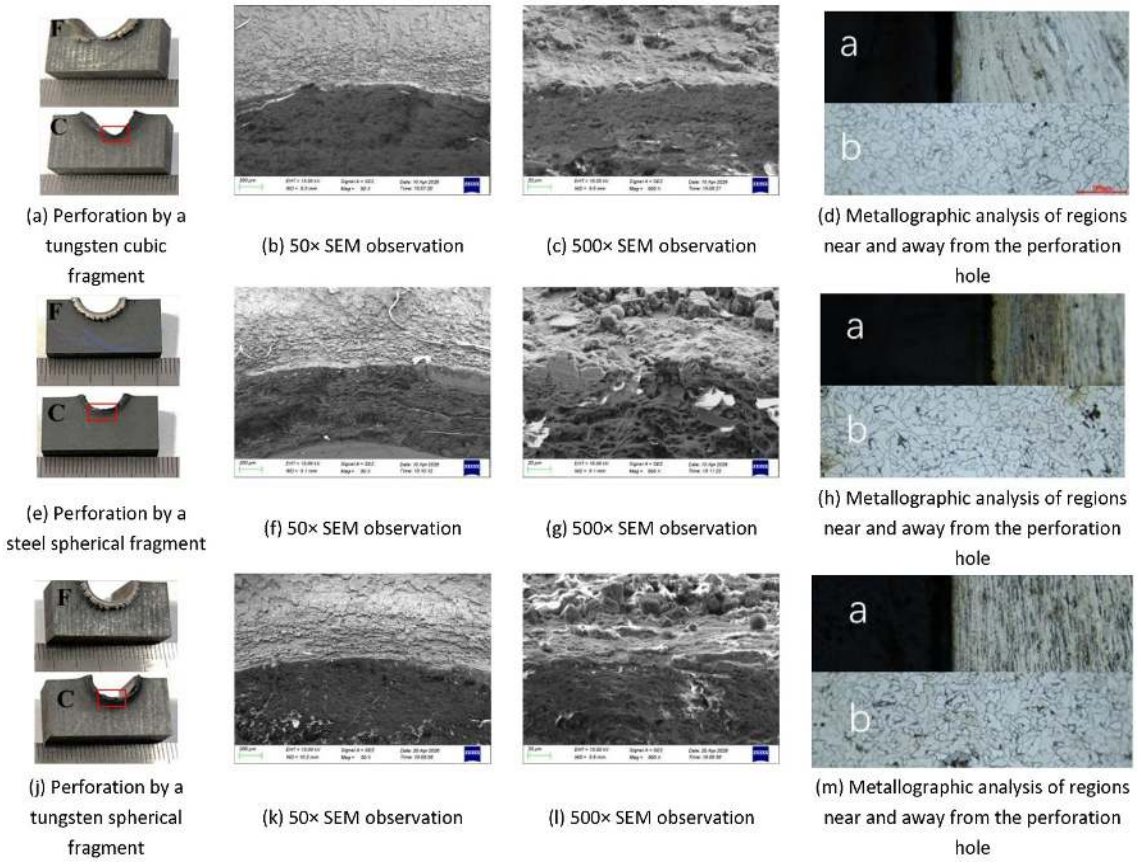


Figure 6. Perforation analysis of the three fragment types against the Q235 plate

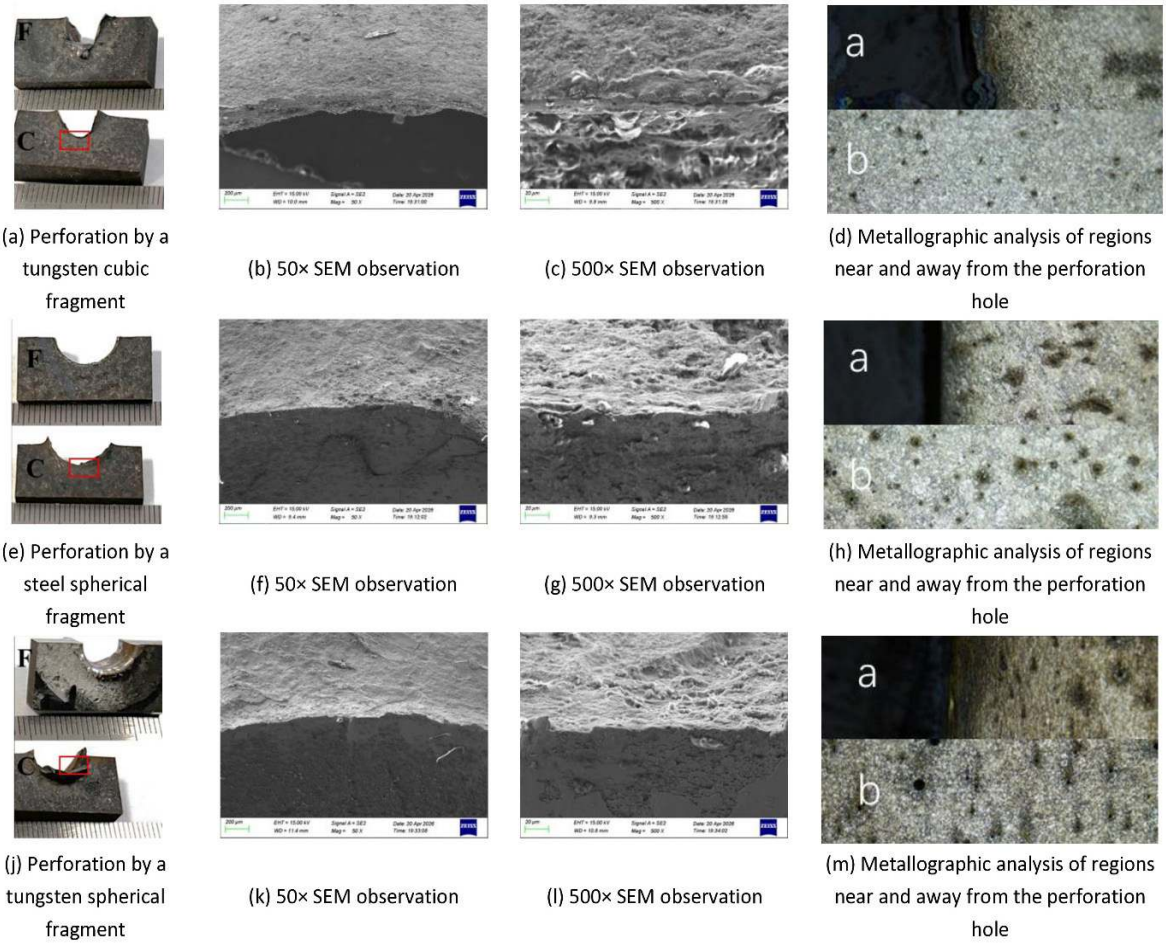


Figure 7. Perforation analysis of the three fragment types against the 616 plate

The fragment-shape effect is also evident. Holes produced by tungsten block fragments generally show stronger asymmetry, with clearer local cutting marks and directional damage along the edge. Steel spheres produce relatively regular hole contours and more prominent plastic hole expansion. Tungsten spheres retain a spherical-contact feature, but because their local load is more concentrated, their exit-side deformation is usually more compact than that produced by steel spheres. These observations indicate that, at comparable scale, angular fragments more readily cause nonuniform contact and local stress concentration, thereby giving the hole-edge failure a stronger directional character; hole evolution under spherical fragments is comparatively more stable.

SEM observations further reveal local fracture features on the exit side. For Q235 steel, the exit-hole edge is generally rough, with evident tearing ridges, plastic-flow traces and ductile-fracture features. The material therefore remains dominated by ductile deformation during perforation, while local shear and ductile tearing jointly contribute to fracture. Under tungsten-block impact, the hole-edge surface shows stronger undulation and directionality, whereas the surfaces produced by steel spheres and tungsten spheres are more continuous. For 616 armor steel, the exit-hole edge is denser and smoother than that of Q235 steel. Coarse plastic-flow traces are much less obvious, while local shear steps, small crack-initiation sites and localization traces are clearer, indicating a more shear-dominated exit-side failure mode in this high-strength steel. Exit-side SEM morphology alone is not sufficient to confirm whether adiabatic shear instability was fully formed. Even so, the degree of hole-edge localization and surface features indicate a stronger tendency toward shear localization in 616 armor steel. For LY12 aluminum alloy, the SEM images show pronounced plastic-flow bands, ductile tearing and local microvoid coalescence, indicating that exit-side material removal is mainly accomplished through plastic hole enlargement and ductile tearing. The asymmetry and local cutting marks are most evident under tungsten block fragments impact, whereas steel spheres and tungsten spheres produce a more continuous hole expansion.

The metallographic observations are consistent with the macroscopic and SEM results. In Q235 steel, the base-material region away from the hole remains relatively intact, whereas the near-hole region shows elongated, bent and locally streamlined microstructural features. This indicates substantial plastic flow and shear deformation on the exit side, but the disturbed zone is limited; the overall response is local shear tearing superposed on plastic hole enlargement. In 616 armor steel, the microstructural difference between the near-hole and far-field regions is concentrated close to the hole edge, with local compaction, stronger deformation orientation and more obvious banded deformation.

The far-field microstructure remains close to its original state. Thus, the disturbed zone is narrower in 616 armor steel under impact loading, but the local deformation is more concentrated, consistent with its compact hole and suppressed plastic petalling. Its exit-side failure is therefore more shear-dominated. In LY12 aluminum alloy, the near-hole region displays more pronounced flow-line morphology and a wider plastic affected zone, while the far-field region remains relatively uniform. The aluminum alloy therefore undergoes more extensive plastic flow and material redistribution on the exit side. Under tungsten block fragments impact, the near-hole microstructure shows stronger nonuniform deformation and local-flow traces, indicating that edge contact further amplifies local flow and tearing in the low-resistance aluminum alloy. Overall, Q235 steel exhibits plastic hole expansion combined with local shear tearing; 616 armor steel shows a stronger tendency toward shear localization; and LY12 aluminum alloy is dominated by ductile hole enlargement and tearing under large-scale plastic flow. Fragment shape clearly modulates the local failure response. Tungsten block fragments more readily cause asymmetric edge failure and local cutting marks, while spherical fragments produce more regular exit-hole contours. For the same spherical shape, tungsten spheres generally produce more concentrated local loading than steel spheres. These phenomena demonstrate that exit-side failure after perforation is not governed by target strength alone; it is jointly controlled by target mechanical properties, fragment shape and local contact loading mode. The exit-side morphology and dominant failure characteristics for different fragment-target combinations are summarized in Table 6.

Table 6 Exit-side morphology and dominant failure modes for fragment-target combinations.

Target / Fragment type	Tungsten block	Steel sphere	Tungsten sphere
Q235 steel	Local shear tearing on the basis of plastic hole enlargement; strong exit-hole asymmetry	Plastic hole enlargement and ductile tearing are evident; relatively regular hole profile	Local shear enlargement and ductile tearing coexist; localized loading is stronger than that of steel spheres
616 armor steel	Pronounced shear localization; compact hole; clear local cutting traces	Shear-dominated perforation accompanied by limited plastic expansion	More evident local shear-dominated features; higher degree of hole-edge localization
LY12 aluminum alloy	Large plastic flow accompanied by local tearing/cutting; strongest exit-hole asymmetry	Plastic hole enlargement and ductile tearing are evident; relatively smooth hole profile	Concentrated plastic hole enlargement dominates, accompanied by ductile tearing; loading is more localized than that of steel spheres

4 ANALYSIS AND DISCUSSION

4.1 Modified penetration model based on dimensional analysis

The classical De Marre formula is mainly applicable to penetration problems involving large-mass projectiles, whereas the Recht–Ipson formula is more suitable for thin-plate perforation. Neither formulation can simultaneously account for the combined effects of small-scale fragments, multi-material target plates, and fragment-shape differences (Masri, 2022). Therefore, instead of directly adopting traditional empirical formulas, this study identifies the key variables governing the penetration process through dimensional analysis and then constructs a power-law semi-empirical perforation model based on the experimental data within the scope of the present tests. In this study, mass [M], length [L], and time [T] are taken as the fundamental dimensions. The main variables include the fragment mass m (g), fragment density ρ_p(g/cm^3), target thickness h (mm), target density ρ_t(g/cm^3), target material strength Y (MPa), characteristic fragment dimension d, and fragment shape factor ψ. The following functional relationship can then be obtained:

$$V_{50} = \sqrt{\frac{Y}{\rho_t}} \cdot f\left(\frac{h}{d}, \frac{m}{\rho_p d^3}\frac{\rho_p}{\rho_t}, \psi\right) \tag{1}$$

Considering geometric similarity, inertial effects, material density ratio, target resistance, and impact obliquity, the ballistic limit velocity is expressed in a unified form as:

$$V_{50} = C \cdot \psi \cdot \left(\frac{h}{d}\right)^{\alpha} \left(\frac{m}{d^3}\right)^{\beta} \left(\frac{\rho_p}{\rho_t}\right)^{\gamma} \left(\frac{Y}{\rho_t}\right)^{k} \tag{2}$$

where C is a dimensional fitting coefficient; α, β, γ, *k* the remaining exponents are parameters to be determined; *f(ϑ)* is the angular term represents the obliquity correction factor; and ψ denotes the shape factor. Equation (2) is not a strictly closed-form analytical expression directly derived from dimensional analysis. Rather, it is a semi-empirical unified model constructed according to the variable combinations identified by dimensional analysis, with its coefficients and exponents further determined by regression of the experimental data. By taking the logarithm of Eq. (2) and performing multiple linear regression, a unified prediction model applicable to normal or oblique penetration of 616 steel, Q235 steel, and LY12 aluminum alloy by steel spheres, tungsten spheres, and tungsten block fragments is obtained:

$$V_{50} = 1473 \cdot \left(\frac{h}{d}\right)^{0.751} \left(\frac{m}{d^3}\right)^{0.156} \left(\frac{\rho_p}{\rho_t}\right)^{-0.661} \left(\frac{Y}{\rho_t}\right)^{0.109} \cdot \psi \tag{3}$$

For spherical fragments, the characteristic dimension *d* is defined as the fragment diameter, which has a clear geometric meaning and is essentially independent of impact attitude. For tungsten block fragments, *d* denotes the nominal contact side length of the block. This value reflects the primary geometric scale of the tungsten block fragment, but it cannot fully describe the differences among face-on, edge-on, corner-on, and deflected contact conditions. The resulting local contact deviation and data scatter are reflected in the present model through the shape factor, residual correction term, and model error. Therefore, Eq. (3) should be regarded as an engineering statistical model for equivalent conversion involving typical fragments. Here, ψ = 1 for spherical fragments, and ψ = 0.922 for tungsten block fragments.

4.2 Correction of morphology-material coupling effects based on residual learning

In Section 4.1, a unified prediction model for the ballistic limit velocity was developed based on dimensional analysis by incorporating the density ratio, target-strength ratio, dimensionless thickness, mass scale, and shape factor, thereby extracting the global scaling law of the penetration process. The baseline model can reflect the average scaling relationship between different fragments and target materials. However, the shape factor is still introduced into the model as a globally equivalent parameter, making it difficult to fully describe the differences between the local contact state of block-shaped fragments and the failure response of target materials. Based on the ballistic limit velocity data in Section 3.1 and the failure morphology analysis in Section 3.2, it can be observed that tungsten block fragments induce different exit-side failure modes in different target materials, and the uncertainty in impact attitude leads to variations in contact conditions. Meanwhile, steel spheres, tungsten spheres, and tungsten block fragments exhibit distinctly different penetration thresholds within the same thickness range.

Therefore, relying solely on a unified shape factor is insufficient to fully describe the coupled effects among fragment material, fragment morphology, and target type. This limitation is the fundamental reason for the systematic bias of the baseline model under certain local test conditions. To further decompose this nonlinear coupling effect, the concept of residual learning is introduced in this study.

Building upon the baseline model developed in Section 4.1, a white-box correction term was further introduced. Let $V_{50}^{(0)}$ denote the theoretical prediction obtained from the dimensional-analysis-based baseline model in Section 4.1, and let *V50* test denote the experimentally fitted ballistic limit velocity derived from the ballistic test results in Tables 3–5. The logarithmic residual between them is defined as:

$$\Delta = \ln\left(V_{50test}\right) - \ln\left(V_{50}^{(0)}\right) \tag{4}$$

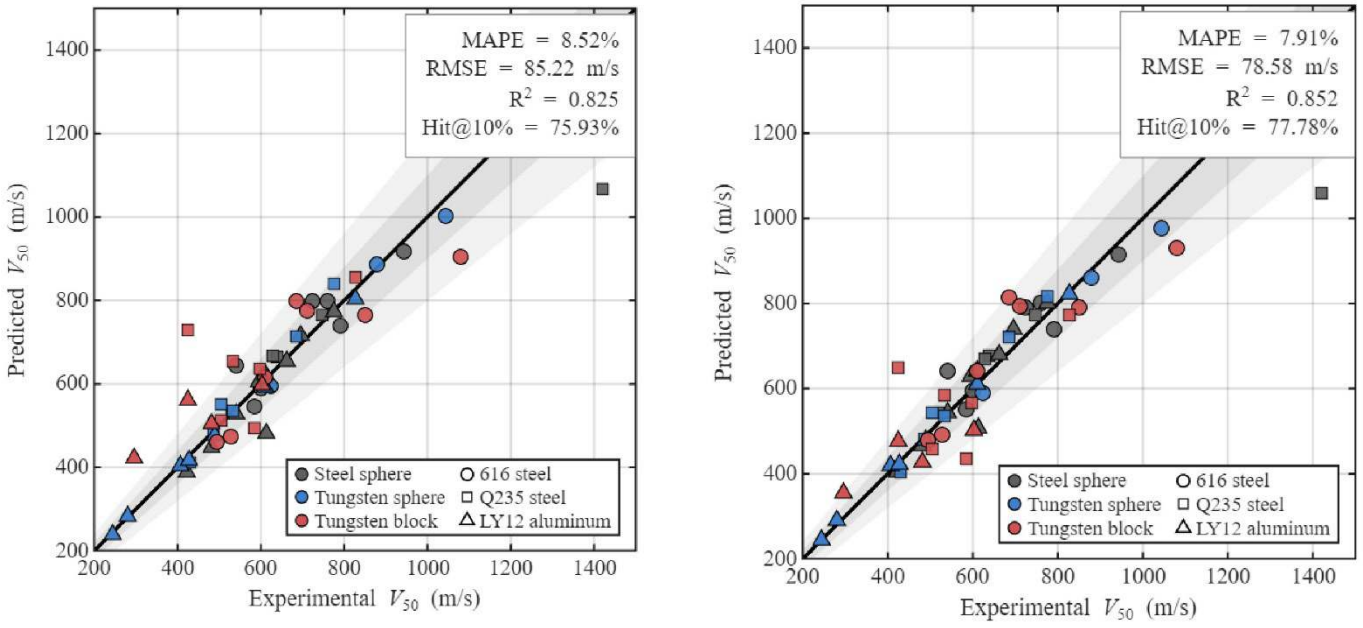
The logarithm of dimensionless thickness *ln(h/d)* and the logarithm of mass *ln(m)* are selected as continuous features. Indicator variables are constructed to represent fragment material, fragment morphology, and target category. The fragment material indicator I_w is set to 1 for tungsten and 0 for steel. The shape indicator I_{block} is set to 1 for tungsten block fragments and 0 for tungsten spheres. The target indicators I_{616} and I_{LY12} are set to 1 when the target is 616 steel or LY12 aluminum alloy, respectively, and 0 otherwise. The steel sphere-Q235 steel condition is taken as the reference group; that is, when the fragment is a steel sphere and the target is Q235 steel, $I_w = 0$, $I_{block} = 0$, $I_{616} = 0$, and $I_{LY12} = 0$. On this basis, a multiple linear regression with explicit interaction terms is used to reconstruct the white-box residual, yielding the full-sample residual correction model:

$$\Delta = \beta_0 + \beta_1 \ln(m) + \beta_2 \ln\left(\frac{h}{d}\right) + \beta_3 I_w + \beta_4 I_{block} + \beta_5 I_{616} + \beta_6 I_{LY12} + \beta_7 \left(I_{block} \cdot I_{616}\right) + \beta_8 \left(I_{block} \cdot I_{LY12}\right) \tag{5}$$

where $\beta_0 \sim \beta_7$ represents the fitted regression coefficient vector, whose components are 0.03055, −0.01721, −0.01852, −0.01634, −0.10678, −0.01526, 0.03323, 0.16841, and −0.07296, respectively. Based on the predicted residual value $\hat{\Delta}$ obtained from the regression model, the dimensionless coupling correction coefficient K_c is further defined.

After the morphology-material coupling correction, the final predicted ballistic limit velocity is given by:

$$\hat{V}_{50} = V_{50}^{(0)} \cdot K_c = V_{50}^{(0)} \cdot \exp\left(\Delta\right) \tag{6}$$



(a) Baseline model (b) Corrected model

Figure 8. Comparison between experimental and predicted ballistic limit velocities

Table 7 Comparison of percentage errors before and after correction for representative cases

Fragment type	Typical condition	Measured V_{50} (m/s)	Prediction before correction (m/s)	Prediction after correction (m/s)	Error before correction	Error after correction
Steel sphere	616 steel, h=4 mm, d=10 mm, m=4.09 g	585.4	625.3	620.9	6.81%	6.06%
Steel sphere	LY12 Al, h=8 mm, d=10 mm, m=4.09 g	481.5	516.1	496.1	7.18%	3.03%
Tungsten sphere	LY12 Al, h=6 mm, d=10 mm, m=9.22 g	244.0	248.3	243.8	1.75%	0.10%
Tungsten sphere	Q235 steel, h=14 mm, d=9 mm, m=6.73 g	776.4	839.5	817.3	8.13%	5.27%
Tungsten block	616 steel, h=8 mm, d=7 mm, m=4.00 g	851.4	764.1	790.7	10.25%	7.13%
Tungsten block	Q235 steel, h=8 mm, d=7 mm, m=4.00 g	597.9	636.8	630.4	6.51%	5.43%

As shown in Figure 8, the baseline model can reasonably describe the overall distribution trend of the samples, indicating that the dimensional-analysis model effectively captures the dominant effects of density ratio, strength ratio, thickness scale, and mass scale. However, for tungsten block fragments and low-resistance target materials, some samples still deviate noticeably from the line of perfect agreement. After introducing the residual correction, the scatter points move closer to the diagonal as a whole, and several samples with large original deviations are compensated to some extent. This indicates that the corrected model can effectively characterize local morphology-material coupling effects while preserving the main scaling law of the baseline model. Table 7 further shows that the improvement is not uniform across all samples, but is mainly reflected in selected high-deviation conditions. Therefore, the corrected model should be understood as a compensation framework that improves overall fitting ability and engineering robustness. Figure 7 shows that, after introducing the residual correction, the predicted results are generally closer to the experimental values than those obtained from the baseline model. This indicates that it is effective to further account for the coupled deviations associated with fragment material, fragment geometry, and target-material category on the basis of the dimensionally informed semi-empirical model. To examine the potential collinearity caused by the simultaneous inclusion of continuous features and indicator variables in the regression model of Eq. (5), a variance inflation factor (VIF) analysis was further performed. The results show that the VIF values of all input variables range from 1.44 to 3.40, which are all below the commonly used threshold of 5. This indicates that the present variable set does not suffer from severe multicollinearity and that the model has acceptable numerical stability.

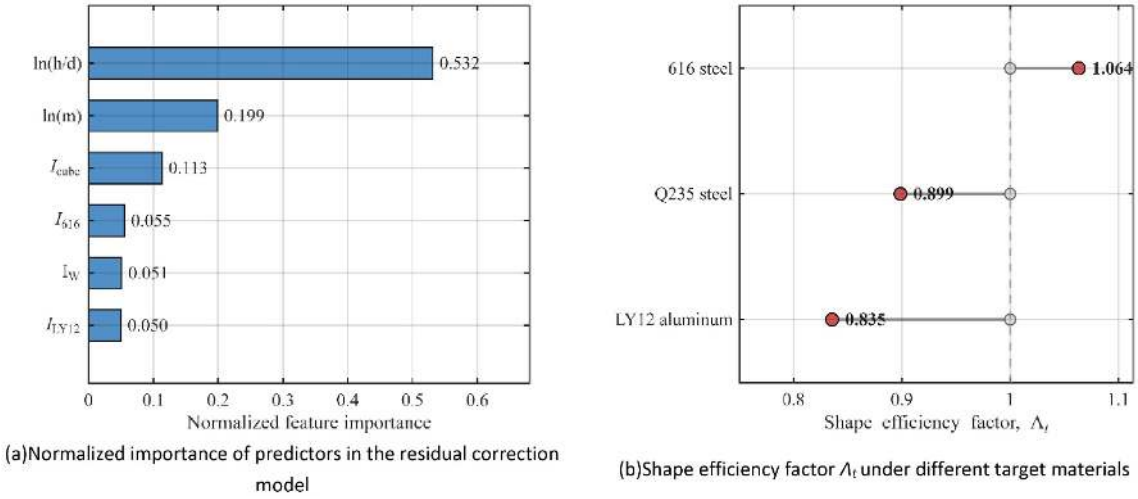
Further coefficient-significance analysis shows that, owing to the limited sample size and the restricted coverage of test conditions, the 95% confidence intervals of some residual terms remain relatively wide. Therefore, individual regression coefficients should not be directly interpreted as independent and deterministic physical parameters. Nevertheless, in terms of sign and relative magnitude, the interaction terms associated with tungsten block fragments show clear physical consistency. The positive value of the ($I_{block} \times I_{616}$) term indicates that the impact of tungsten block fragments on 616 armor steel is more likely to correspond to a higher local energy-dissipation resistance. In contrast, the negative value of the ($I_{block} \times I_{LY12}$) term suggests that the impact of tungsten block fragments on LY12 aluminum alloy tends to reduce the equivalent anti-perforation capability. This trend is consistent with the target-response differences revealed by the preceding analyses of macroscopic perforation morphology, exit-side SEM observations, and metallographic characterization near the perforation region. Therefore, the residual correction terms are not merely data-fitting compensations; rather, they reflect, to some extent, the local coupling relationship between fragment geometry and target response. To further evaluate the generalization capability of the model, leave-one-out cross validation (LOOCV) was conducted using the full dataset. The corrected model gives a MAPE of 9.70%, an RMSE of 96.42 m/s, an (R^2) of 0.776, and a prediction coverage of 72.22% within the ±10% error band under cross-validation conditions. Although the cross-validation accuracy is lower than the in-sample fitting accuracy, the model still maintains good predictive consistency. This suggests that the proposed model has a certain degree of engineering generalizability within the range of typical fragment types, target-material systems, and impact velocities covered in this study.

To quantify the morphology effect more intuitively, a morphology efficiency coefficient Λ_t is further defined. This coefficient characterizes the corrected penetration efficiency of tungsten block fragments relative to tungsten spheres under the same tungsten material, the same mass, and the same dimensionless thickness for different target materials.

$$\begin{aligned}\Lambda_{616} &= \exp\left(b_{block} + b_{block\times 616}\right)\\ \Lambda_{Q235} &= \exp\left(b_{block}\right)\\ \Lambda_{LY12} &= \exp\left(b_{block} + b_{block\times LY12}\right)\end{aligned} \tag{7}$$

Where b_{block}, $b_{block\times 616}$, and $b_{block\times LY12}$ are the regression coefficients corresponding to the main effect of fragment morphology and its interaction effects with different target materials in the residual model, respectively.

According to the current full-sample regression results, Λ_{616} approximately equals 1.064, Λ_{Q235} approximately equals 0.899, and Λ_{LY12} approximately equals 0.836.



(a)Normalized importance of predictors in the residual correction model

(b)Shape efficiency factor Λ_t under different target materials

Figure 9. Interpretability analysis of the residual correction model

Figure 9(a) shows the normalized importance of the input features in the residual model. The results indicate that *ln(h/d)* remains the most important control variable at the residual level, followed by *ln(m)*. Thus, after the baseline model has absorbed the main dimensional scaling laws, thickness scale and mass scale still dominate the distribution of local deviations. I_W, I_{block}, I_{616} and I_{LY12} mainly act as directional correction variables. Figure 9(b) presents the morphology efficiency factor Λ_t for different target materials. For 616 steel, $\Lambda_{616} > 1$, indicating that, for tungsten fragments of the same material, tungsten block fragments more readily induce high-energy shear plugging in high-strength steel. The corrected model therefore needs to increase the corresponding ballistic limit velocity. For Q235 steel and LY12 aluminum alloy, Λ_t is less than 1, and Λ_{LY12} is the lowest, this indicates that tungsten block fragments are more likely to induce localized cutting, hole enlargement, or tearing responses. These findings are consistent with the exit-side failure characteristics identified from the macroscopic morphology, SEM observations, and metallographic analysis presented in Section 3.2.

4.3 Derivation of equivalent conversion coefficients

In the design of multi-material composite protective structures and in target vulnerability assessment, a high-confidence equivalent thickness conversion relationship between target materials is a central engineering requirement. Based on the unified ballistic-limit prediction model established above, this section derives the ideal conversion coefficient and then uses the experimental data to correct its coupled disturbance under complex physical conditions.

4.3.1 Ideal equivalent solution based on dimensional analysis

From Eq. (6), for a given fragment types (spherical or cubic), given fragment parameters (m, d, ρ, p, ψ) and a given incidence angle θ, the expression can be rearranged as:

$$V_{50} = \tilde{C}_s \exp\left(\mu_t^{(s)}\right)\left(\frac{h}{d}\right)^{0.732}\left(\frac{\rho_p}{\rho_t}\right)^{-0.661}\left(\frac{Y}{\rho_t}\right)^{0.109} \tag{8}$$

where *t* denotes the target material category, and $\tilde{C}_s$ is a constant determined only by the fragment type and the shared experimental conditions.

The target–morphology correction term $\mu_t^{(s)}$ takes the following values:

For spherical fragments, $\mu_{616}^{(shere)} = -0.01526, \mu_{Q235}^{(shere)} = 0, \mu_{LY12}^{(shere)} = 0.03323$

For tungsten block fragments, $\mu_{616}^{(block)} = 0.15315, \mu_{Q235}^{(block)} = 0, \mu_{LY12}^{(block)} = -0.03973$

Based on the concept of equivalent ballistic resistance, for a given fragment threat, if materials *A* and *B* have identical ballistic limit velocities, i.e., then the corresponding equivalent thickness relationship between the two materials can be written as:

$$\exp\left(\mu_A^{(s)}\right)h_A^{0.732}\rho_A^{0.552}Y_A^{0.109} = \exp\left(\mu_B^{(s)}\right)h_B^{0.732}\rho_B^{0.552}Y_B^{0.109} \tag{9}$$

The equivalent thickness conversion coefficient from material A to material B is further defined as $k_{A\to B}^{(s)} = h_B / h_A$

Thus:

$$k_{A\to B}^{(s)} = \left[\exp\left(\mu_A^{(s)} - \mu_B^{(s)}\right)\left(\frac{\rho_A}{\rho_B}\right)^{0.552}\left(\frac{Y_A}{Y_B}\right)^{0.109}\right]^{\frac{1}{0.732}} \tag{10}$$

where *s* denotes the fragment-morphology category.

4.3.2 Fragment-type-specific statistical equivalent coefficients and engineering expression

Although Section 4.3.1 derived the analytical equivalent-thickness conversion coefficients among different materials based on the corrected ballistic-limit velocity model, an engineering statistical cross-check using discrete experimental data remains necessary. This is because the experimental data inevitably involve sample scatter, finite-sample fluctuations, and local deviations induced by morphology–material coupling. For any two target materials, *A* and *B*, with the fragment type denoted as s, the ballistic limit velocity of material A at the i-th representative thickness sample point is first calculated according to Eq. (6):

$$\hat{V}_{50,A}\left(h_{A,i}, m_i, d_i, \theta_i\right).$$

The equivalent thickness $h_{B,i}^{eq}$ of material *B* corresponding to the same ballistic limit velocity is then obtained from the equal-velocity condition:

$$\hat{V}_{50,B}\left(h_{B,i}^{eq}, m_i, d_i, \theta_i\right) = V_{50,A}\left(h_{A,i}, m_i, d_i, \theta_i\right) \tag{11}$$

The equivalent coefficient corresponding to the i-th representative thickness point is then defined as:

$$\eta_{A\to B,i}^{(s)} = \frac{h_{B,i}^{eq}}{h_{A,i}} \tag{12}$$

If all representative thickness points for fragment type s are denoted as i = 1, 2, ..., n_s, the statistical mean equivalent coefficient from material A to material B under that fragment type is defined as:

$$\bar{\eta}_{A\to B}^{(s)} = \frac{1}{n_s}\sum_{i=1}^{n_s}\eta_{A\to B,i}^{(s)} \tag{13}$$

Its fluctuation range is defined as:

$$\left(\overline{\eta}^{(s)}_{A\to B,\min}=\min\left(\eta^{(s)}_{A\to B,i}\right),\overline{\eta}^{(s)}_{A\to B,\max}=\max\left(\eta^{(s)}_{A\to B,i}\right)\right) \tag{14}$$

When the fragment type is unknown or the fragment shapes are widely distributed, a mixed-fragment threat can be considered by expanding the fluctuation range. Let the fragment types be s_1, s_2, ..., s_n. Using Eq. (10), engineering recommended intervals can be further established on the basis of analytical values and statistical ranges for different morphology categories:

$$\begin{aligned}&\left(\overline{\eta}^{\min}_{A\to B},\overline{\eta}^{\max}_{A\to B}\right)\\&\overline{\eta}^{\min}_{A\to B}=\min\left(\overline{\eta}^{s_1}_{A\to B},\overline{\eta}^{s_2}_{A\to B},...,\overline{\eta}^{s_n}_{A\to B}\right)\\&\overline{\eta}^{\max}_{A\to B}=\max\left(\overline{\eta}^{s_1}_{A\to B},\overline{\eta}^{s_2}_{A\to B},...,\overline{\eta}^{s_n}_{A\to B}\right)\end{aligned} \tag{15}$$

Because steel spheres and tungsten spheres share the same spherical center matrix in the analytical sense, two separate spherical center matrices are not provided. Instead, a spherical-fragment equivalent matrix and a cubic-fragment equivalent matrix are established. To further quantify the modulation of equivalent conversion by morphology, Table 10 summarizes the spherical analytical values, cubic analytical values and recommended engineering intervals. Substituting the density and strength parameters of the three target materials into Eq. (10) gives the analytical equivalent thickness conversion matrices for typical materials under spherical-fragment and cubic-fragment conditions. Since steel spheres and tungsten spheres share the same spherical center values analytically, Tables 8 and 9 present the spherical and cubic matrices, respectively.

Table 8 Equivalent thickness conversion coefficients of typical metallic targets under spherical-fragment impact.

Source material / Target material	616 steel	Q235 steel	LY12 Al
616 steel	1.00	1.26	2.50
Q235 steel	0.80	1.00	1.99
LY12 Al	0.40	0.50	1.00

Table 9 Equivalent thickness conversion coefficients of typical metallic targets under tungsten block fragments impact.

Source material / Target material	616 steel	Q235 steel	LY12 Al
616 steel	1.00	1.58	3.48
Q235 steel	0.63	1.00	2.20
LY12 Al	0.29	0.45	1.00

Tables 8-10 give the equivalent conversion relationships for typical materials under different fragment morphologies. Each matrix element represents the equivalent thickness ratio when a source material is converted into a target material.

Table 10 Conversion relationships, morphology sensitivity and recommended intervals based on the corrected model.

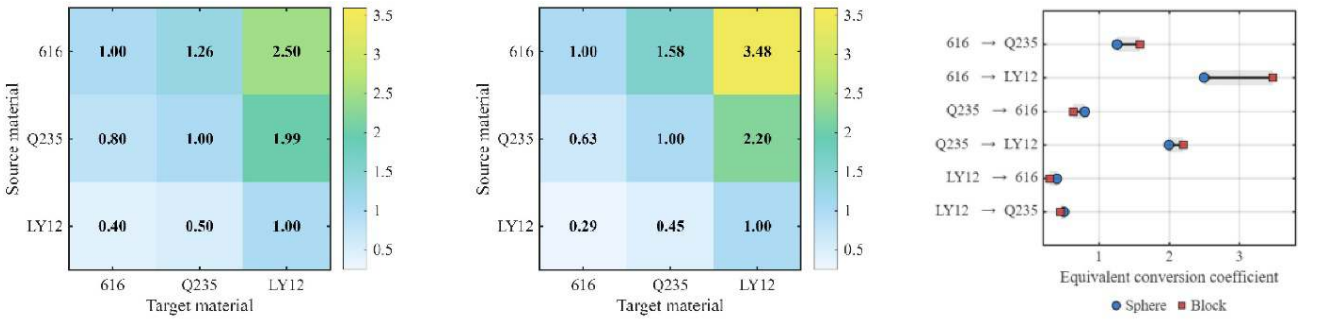
Conversion path	Spherical analytical value	Cubic analytical value	Engineering recommended interval	Maximum shape deviation (%)
616 → Q235	1.26	1.58	1.26-1.58	25.85
616 → LY12	2.50	3.48	2.50-3.48	39.03
Q235→ 616	0.80	0.63	0.63-0.80	20.54
Q235 → LY12	1.99	2.20	1.99-2.20	10.47
LY12 → 616	0.40	0.29	0.29-0.40	28.07
LY12 → Q235	0.50	0.45	0.45-0.50	9.48

The maximum deviation is defined as follows:

$$\varepsilon_{\max}=\frac{\left|k^{cude}-k^{sphere}\right|}{k^{shere}}\times 100\%\cdot$$

The maximum shape deviation, defined as the relative discrepancy between the analytical values under spherical and cubic impacts, serves to quantify the morphological sensitivity of the equivalent conversion laws. Table 10 indicates that the conversion paths between 616 steel and LY12 aluminum alloy (i.e., 616 → LY12 and LY12 → 616) exhibit the highest morphological sensitivity. Specifically, the equivalence coefficient for the 616 → LY12 conversion escalates from 2.50 under spherical impact to 3.48 under cubic impact, yielding a maximum shape deviation of 39.03%. Conversely, the reciprocal path (LY12 → 616) drops from 0.40 to 0.29, corresponding to a shape deviation of 28.07%. This substantiates that for material pairings with pronounced strength gradients, sharp-edged projectiles severely exacerbate the directional asymmetry of the scaling relationship. By contrast, the shape deviations for the Q235 ↔ LY12 paths remain relatively marginal, implying that morphological sensitivity is attenuated under moderate target strength gradients compared to the extreme 616/LY12 combination. Within the proposed residual compensation framework, cross-material equivalent thickness scaling transcends a static scalar dictated merely by density and strength ratios; rather, it is heavily governed by the dynamic coupling between fragment morphology and the transient target response.

Supported by data analysis and visual mapping, it is conclusively established that equivalent conversions within multi-material systems possess profound morphological sensitivity and inherent directional asymmetry.



(a) Equivalent conversion coefficient heatmap for sphere projectiles

(b) Equivalent conversion coefficient heat map for block projectiles

(c) Equivalent conversion coefficient interval comparison plot

Figure 10. Equivalent thickness conversion coefficients and morphology sensitivity under spherical- and cubic-fragment conditions

Figures 10(a) and 10(b) present the equivalent thickness conversion coefficient matrices for spherical and tungsten block fragments, respectively, using the same color scale. The comparison shows that tungsten block fragments substantially amplify the conversion difference between strong and weak target materials. Figure 10(c) summarizes the spherical and cubic analytical values for six representative conversion paths. The 616 steel ↔ LY12 aluminum alloy pair is the most sensitive to fragment morphology. Under cubic-fragment impact, the conversion coefficients are either clearly increased or decreased relative to the spherical-fragment case, indicating that angular fragments strengthen the asymmetry of material conversion. The difference between Q235 steel and LY12 aluminum alloy is comparatively limited, showing weaker morphology sensitivity under a moderate strength gradient.

5 CONCLUSIONS

To address the influence of fragment type in equivalent thickness conversion for typical metallic targets, ballistic limit tests were conducted using steel spheres, tungsten spheres, and tungsten block fragments against 616 armor steel, Q235 steel and LY12 aluminum alloy. Together with exit-side morphology characterization, a dimensional-analysis model and a residual correction method, fragment-morphology-specific equivalent thickness conversion relationships were established. The main conclusions are as follows:

(1) Within the present test range, the *V50* data for three fragment types and three target materials show that target perforation resistance is governed not only by target strength and density, but also by fragment mass, characteristic size, material density and contact morphology. At comparable thickness and mass scales, tungsten block fragments more readily form localized concentrated loading because of edge contact and higher sectional kinetic-energy density. Equivalent thickness therefore cannot be calculated simply from a static strength ratio or density ratio.

(2) Macroscopic perforation, SEM and metallographic results reveal distinct failure responses among the three targets. Q235 steel mainly shows plastic hole expansion accompanied by local shear tearing. The hole in 616 armor steel is more compact, with a more evident shear-dominated character. LY12 aluminum alloy is dominated by wide-range plastic flow, hole-edge curling and ductile tearing. Edge contact by tungsten block fragments amplifies local stress concentration and directional cutting, causing the same target material to exhibit different perforation mechanisms under different fragment morphologies.

(3) The equivalent thickness conversion matrices show that the equivalent coefficient for the same target-material pair changes markedly with fragment type. For example, when 616 steel is converted to LY12 aluminum alloy, the equivalent coefficient is 2.50 under spherical-fragment impact and increases to 3.48 under tungsten block fragments impact, giving a maximum shape deviation of 39.03%. The coefficient for conversion from 616 steel to Q235 steel increases from 1.26 to 1.58, and that from Q235 steel to LY12 aluminum alloy increases from 1.99 to 2.20. The greater the strength difference between materials, the more sensitive the equivalent coefficient becomes to fragment morphology. The conversion path between 616 steel and LY12 aluminum alloy should therefore be treated as a key correction case in engineering thickness conversion.

(4) When the fragment type is clearly defined, the equivalent conversion coefficient corresponding to that morphology should be used. When fragment morphology is uncertain in damage assessment, the engineering recommended interval formed by the spherical and cubic results should be adopted. Future work may further calibrate this coefficient system by expanding the sample size and introducing oblique impact and multilayer target conditions.

Author's Contribuitions: Writing-original draft, Chuanyun Tao; Writing-review&editing, Chuanyun Tao and Weihang Li; Conceptualization, Zheng Yu; Funding acquisition, Wenbin Li; Supervision, Peng Chen and Ning Jiang. All authors have read and agreed to the published version of the manuscript

Data availability statement: Research data is available in the body of the article. Additional supporting data are available from the corresponding author upon reasonable request.

Editor: Marcilio Alves

References

Atoui, O., Maazoun, A., Aminou, A. et al. (2023). Dynamic behavior of aluminum plates subjected to sequential fragment impact and blast loading: An experimental study. Applied Sciences 13(6):3542.

Børvik, T., Dey, S., Clausen, A.H. (2009). Perforation resistance of five different high-strength steel plates subjected to small-arms projectiles. International Journal of Impact Engineering 36(7):948-964.

Cheng, J.C., Zhang, S., Liu, Q., Ye, S.J., Luo, S.N., Cai, Y., Huang, J.Y. (2022). Ballistic impact experiments and modeling on impact cratering, deformation and damage of 2024-T4 aluminum alloy. International Journal of Mechanical Sciences 231:107312.

Cheng, J.C., Zhao, S.P., Fan, D., Chai, H.W., Ye, S.J., Li, C., Luo, S.N., Cai, Y., Huang, J.Y. (2021). Multiple ballistic impacts on 2024-T4 aluminum alloy by spheres: Experiments and modelling. Journal of Materials Science & Technology 94:164-174.

Deng, Y., Wu, H., Zhang, Y. et al. (2022). Experimental and numerical study on the ballistic resistance of 6061-T651 aluminum alloy thin plates struck by different nose shapes of projectiles. International Journal of Impact Engineering 160:104083.

Deng, Y., Wu, H., Li, H. et al. (2023). Effect of Lode angle and projectile diameter on the ballistic resistance of 6061-T651 aluminum alloy plates struck by hemispherical nosed projectile. European Journal of Mechanics-A/Solids 100:105030.

Dey, S., Børvik, T., Hopperstad, O.S., Leinum, J.R., Langseth, M. (2004). The effect of target strength on the perforation of steel plates using three different projectile nose shapes. International Journal of Impact Engineering 30(8-9):1005-1038.

Du, C., Cao, J., Bai, Y. et al. (2025). Rapid equivalence method for ballistic performance of composite and metallic protective structures. Acta Materiae Compositae Sinica:1-13. http://dx.doi.org/10.13801/j.cnki.fhclxb.20250818.001. (in Chinese)

Du, C., Cao, J., Yejie, Q., Zhao, Z., Zhang, C. (2025). Rationalized equivalence method for high-velocity impacts of composite and metal panels. Composite Structures 357:118910.

Ekanayake, I.U., Meddage, D.P.P., Rathnayake, U. (2022). A novel approach to explain the black-box nature of machine learning in compressive strength predictions of concrete using Shapley additive explanations (SHAP). Case Studies in Construction Materials 16:e01059.

Han, J., Shi, Y., Ma, Q. et al. (2022). Experimental and numerical investigation on the ballistic resistance of 2024-T351 aluminum alloy plates with various thicknesses struck by blunt projectiles. International Journal of Impact Engineering 163:104182.

James, G.R. (2020). Development of models to assess penetrating injury from ballistic projectiles. Ph.D. Thesis, United Kingdom Defence Academy/Cranfield University.

Ji, H., Wang, X., Tang, N. et al. (2024). Ballistic perforation of aramid laminates: Projectile nose shape sensitivity. Composite Structures 330:117807.

Jordan, J.B., Naito, C.J. (2010). Calculating fragment impact velocity from penetration data. International Journal of Impact Engineering 37(5):530-536.

Khan, M., Javed, M.F., Othman, N.A. et al. (2025). Predicting penetration depth in ultra-high-performance concrete targets under ballistic impact: An interpretable machine learning approach augmented by deep generative adversarial network. Results in Engineering 25:103909.

Kılıç, N., Ekici, B., Bedir, S. (2017). Optimization of high hardness perforated steel armor plates using finite element and response surface methods. Mechanics of Advanced Materials and Structures 24(7):615-624.

Kpenyigba, K.M., Jankowiak, T., Rusinek, A. et al. (2013). Influence of projectile shape on dynamic behavior of steel sheet subjected to impact and perforation. Thin-Walled Structures 65:93-104.

Lei, X.D., Wu, X.Q., Zhang, Z., Xiao, K.L., Wang, Y.W., Huang, C.G. (2021). A machine learning model for predicting the ballistic impact resistance of unidirectional fiber-reinforced composite plate. Scientific Reports 11:6503.

Li, H., Zhang, X., Gao, J. (2024). A cloud model target damage effectiveness assessment algorithm based on spatio-temporal sequence finite multilayer fragments dispersion. Defence Technology 40:48-64.

Li, H., Zhang, X. (2024). An equivalent target plate damage probability calculation mathematics model and damage evaluation method. Defence Technology 41:82-103.

Li, H., Zhang, X., Zhang, X. (2020). Calculation model and method of target damage efficiency assessment based on warhead fragment dispersion. IEEE Transactions on Instrumentation and Measurement 70:1-8.

Lomazzi, L., Cadini, F., Giglio, M. (2022). Vulnerability assessment to projectiles: Approach definition and application to helicopter platforms. Defence Technology 18(9):1523-1537.

Masri, R. (2022). Practical formulae for predicting the ballistic limit velocity of armour perforation by ductile hole growth. International Journal of Impact Engineering 167:104219.

Masri, R., Ryan, S. (2023). Ballistic limit predictions of non-identical layered targets perforated in ductile hole formation. International Journal of Impact Engineering 171:104391.

Masri, R., Ryan, S. (2024). Approximate theory of armour perforation by ductile hole expansion. International Journal of Impact Engineering 187:104925.

Mauchant, D., Rice, K.D., Riley, M.A. et al. (2011). Analysis of three different regression models to estimate the ballistic performance of new and environmentally conditioned body armor. U.S. Department of Commerce, National Institute of Standards and Technology.

Mykhailovskyi, D., Skliarov, I., Khomik, M. et al. (2024). Analysis of methods for calculating the penetrating effect of the main types of missiles and fragmentation damage to the structures of protective constructions. Strength of Materials and Theory of Structures 113:171-182.

Noh, D., Fazily, P., Seo, S., Lee, J., Seo, S., Huh, H., Yoon, J.W. (2025). Data driven prediction of fragment velocity distribution under explosive loading conditions. Defence Technology 43:109-119.

Owolabi, G.M., Odeshi, A.G., Singh, M.N.K. et al. (2007). Dynamic shear band formation in Aluminum 6061-T6 and Aluminum 6061-T6/Al2O3 composites. Materials Science and Engineering A 457(1-2):114-119.

Rodríguez-Millán, M., Garcia-Gonzalez, D., Rusinek, A., Abed, F., Arias, A. (2018). Perforation mechanics of 2024 aluminium protective plates subjected to impact by different nose shapes of projectiles. Thin-Walled Structures 123:1-10.

Ryan, S., Sushma, N.M., AV, A.K. et al. (2024). Machine learning for predicting the outcome of terminal ballistics events. Defence Technology 31:14-26.

Ryan, S., Thaler, S., Kandanaarachchi, S. (2016). Machine learning methods for predicting the outcome of hypervelocity impact events. Expert Systems with Applications 45:23-39.

Schonberg, W., Ryan, S. (2022). Predicting metallic armour performance when impacted by fragment-simulating projectiles: Model adjustments and improvements. International Journal of Impact Engineering 161:104090.

Sen, S., Shaw, A., Nayak, S. (2022). A mathematical model for perforation of metal plates through adiabatic shear plugging. International Journal of Impact Engineering 163:104175.

Senthil, K., Iqbal, M.A., Arindam, B., Mittal, R., Gupta, N.K. (2018). Ballistic resistance of 2024 aluminium plates against hemispherical, sphere and blunt nose projectiles. Thin-Walled Structures 126:94-105.

Shin, Y., Chung, J., Kim, J.H. (2018). Test and estimation of ballistic armor performance for recent naval ship structural materials. International Journal of Naval Architecture and Ocean Engineering 10(6):762-781.

Thompson, S., Teixeira-Dias, F., Paulino, M. et al. (2022a). Ballistic response of armour plates using generative adversarial networks. Defence Technology 18(9):1513-1522.

Thompson, S., Teixeira-Dias, F., Paulino, M. et al. (2022b). Predictions on multi-class terminal ballistics datasets using conditional generative adversarial networks. Neural Networks 154:425-440.

Wang, Y., Sun, W. (2024). Machine learning-based real-time velocity prediction of projectile penetration to carbon/aramid hybrid fiber laminates. Thin-Walled Structures 197:111600.

Wu, Y., Lu, W., Ma, M. et al. (2025). Analytical model of the perforation process of spherical-nosed projectiles impacting finite-thickness metal plates. Defence Technology.

Xiao, Y., Wang, H., Fan, C. et al. (2024). Establishment and simulation of an equivalent model for projectile penetration into flat thin target plates. Journal of Vibration and Shock 43(24):243-250. http://dx.doi.org/10.13465/j.cnki.jvs.2024.24.026. (in Chinese)

Xing, B., Du, C., Du, Z. (2022). An intelligent optimization method of trajectory correction projectile based on design of experiments and stochastic kriging. In: 1st International Conference on Mechanical System Dynamics (ICMSD 2022), IET, pp.1493-1503.

Yankelevsky, D.Z., Feldgun, V.R., Karinski, Y.S. (2023). The DISCS method for perforation simulation of thin metallic plates by a rigid projectile. International Journal of Solids and Structures 281:112440.

Yu, Y., Li, X., Niu, Y. et al. (2025). Velocity attenuation of typical steel fragments in snow. Acta Armamentarii 46(S2):296-305. (in Chinese)

Zhang, J., Sun, H., He, J. et al. (2023). Experimental study on penetration of steel rail targets by different types of fragments. Journal of Ordnance Equipment Engineering 44(11):235-239+269. (in Chinese)

Zhang, J., Wu, Z., Zhang, F. et al. (2024). Similarity and equivalent design method for steel plate targets of different materials based on a modified compensation model. Acta Armamentarii 45(04):1297-1310. (in Chinese)

Zhang, X., Li, H. (2022). A target damage assessment mathematical model and calculation method based on the intersection of warhead fragment and target mechanism. Mathematics 10(17):3101.

Zhu, J., Zheng, Y., Li, W. et al. (2019). Axial distribution of fragments from the dynamic explosion fragmentation of metal shells. International Journal of Impact Engineering 123:140-146.

Zhu, Z., Kong, X., Zhou, H. et al. (2025). A hybrid data-driven machine learning framework for predicting the impact resistance of composite armor. International Journal of Impact Engineering 195:105125.